Supporting Information

Charge transfer and chemo-mechanical coupling in respiratory complex I

Chitrak Gupta[1,2], Umesh Khaniya[3,4], Chun Kit Chan[5], Francois Dehez[6], Mrinal Shekhar[5], M. R. Gunner[3,4], Leonid Sazanov[7] (c), Christophe Chipot[5,6] (c), and Abhishek Singharoy[1,2] (c)

1. School of Molecular Sciences, Arizona State University, Tempe, AZ, USA
2. Biodesign Institute, Arizona State University, Tempe, AZ, USA
3. Department of Physics, City College of New York, New York, NY, USA
4. Department of Physics, The Graduate Center of the City University of New York, New York, NY, USA
5. Department of Physics, University of Illinois at Urbana-Champaign, Urbana, USA
6. University of Lorraine, Nancy, France
7. Institute of Science and Technology, Austria

Table of Content

Supporting Results

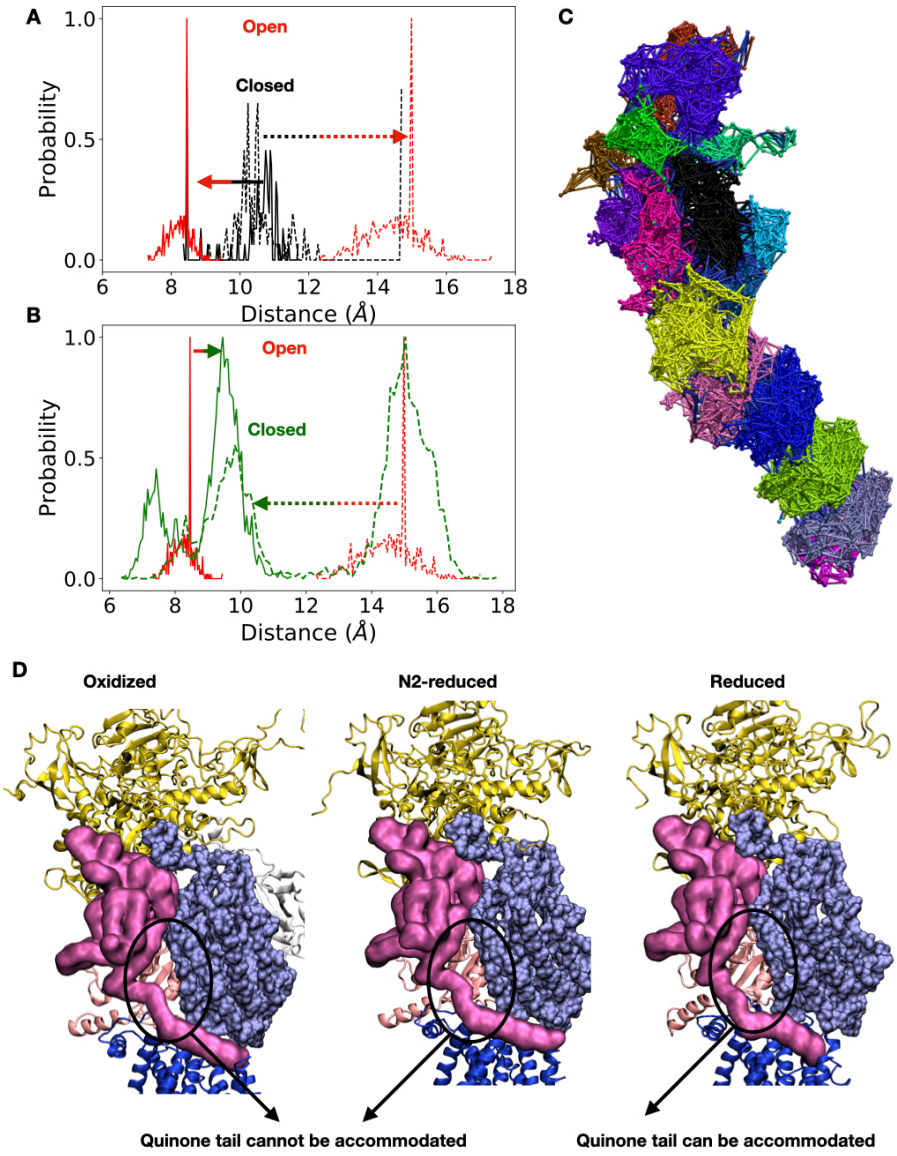

Figure S1: **Distribution of distance between binding site residues of complex I.** **(A)** Peaks (black: oxidized complex I, red: reduced complex I; solid: His38-Asp139 and broken: His38-Tyr87) near 8.5 Å and 15 Å represent the starting conformation, which is the crystal structure. In this structure, the binding site is open, indicated by a large distance between His38 and Tyr87 (site where the quinone head binds) and a small distance between His38 and Asp139. As the 500 ns MD simulation proceeds, oxidized complex I (black) slowly shifts to the peaks near 10 - 11 Å, where the His38 moves away from the Asp139 and comes closer to the Tyr87, closing the binding pocket. **(B)** Starting with the final conformation of the reduced complex I after 500 ns MD (red), simulations were performed with all the Fe-S clusters set to oxidized (green). During this 800 ns simulation, the binding pocket closed. This open-to-close transition is indicated by an increase in the His38-Asp139 distance (solid lines) and concomitant decrease in the His38-Tyr87 distance (broken lines), converging at the distance distributions derived from the oxidized complex

I simulations (shown in black on the left panel). The rate of quinone pocket opening when the reduced complex I is faster than the reverse process in the oxidized complex. The closing event spanned 400 ± 50 ns, marginally longer than the opening transition, which took about 250 ± 30 ns, suggesting that the forward and backward energy transfer pathways do not exactly overlap. Such hysteretic behavior is in line with biochemical measurements, establishing that energy turnover in *Thermus thermophilus* complex I is not completely reversible. **(C)** Dynamical network of the re-oxidized Complex I attributes the entire Nqo4 chain to a single concerted network bereft of hinge-bending movement, similar to that of the oxidized complex I in Figure 4D. **(D)** In order to access the binding site, quinone must accommodate its tail. In oxidized (left) as well as N2-reduced complex I (center), subunit Nqo9 (pink) blocks access to the binding site within subunit Nqo4 (shown in surface representation). Only when all four Fe_4S_4 subunits are reduced (right), the binding site is accessible to the quinone.

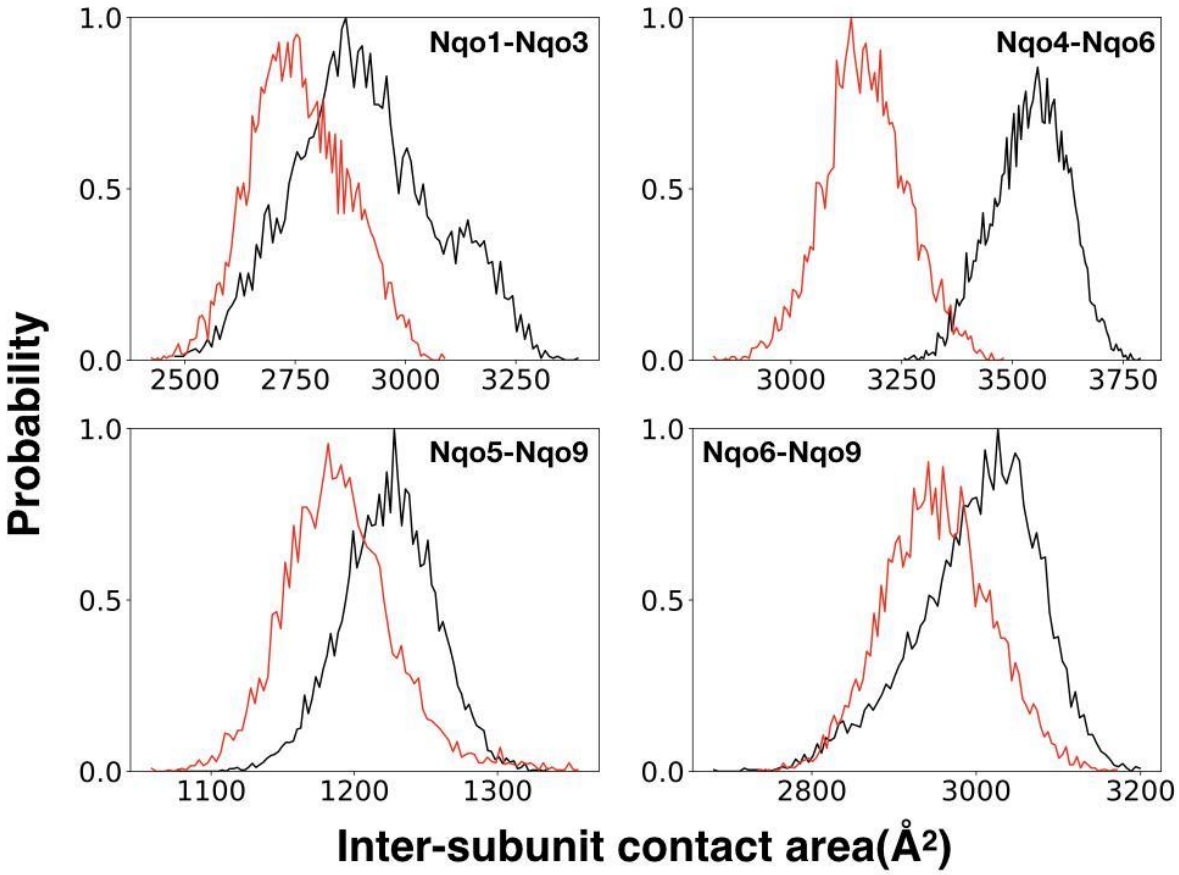

Figure S2: Inter-subunit contact surface area in the oxidized (black) and reduced (red) complex I.

Reduction of the Fe-S clusters causes the subunits to move away from each other, resulting in a decrease of the contact surface area. Mean and standard deviation of the contact surface areas are shown in Figure 2B of main text.

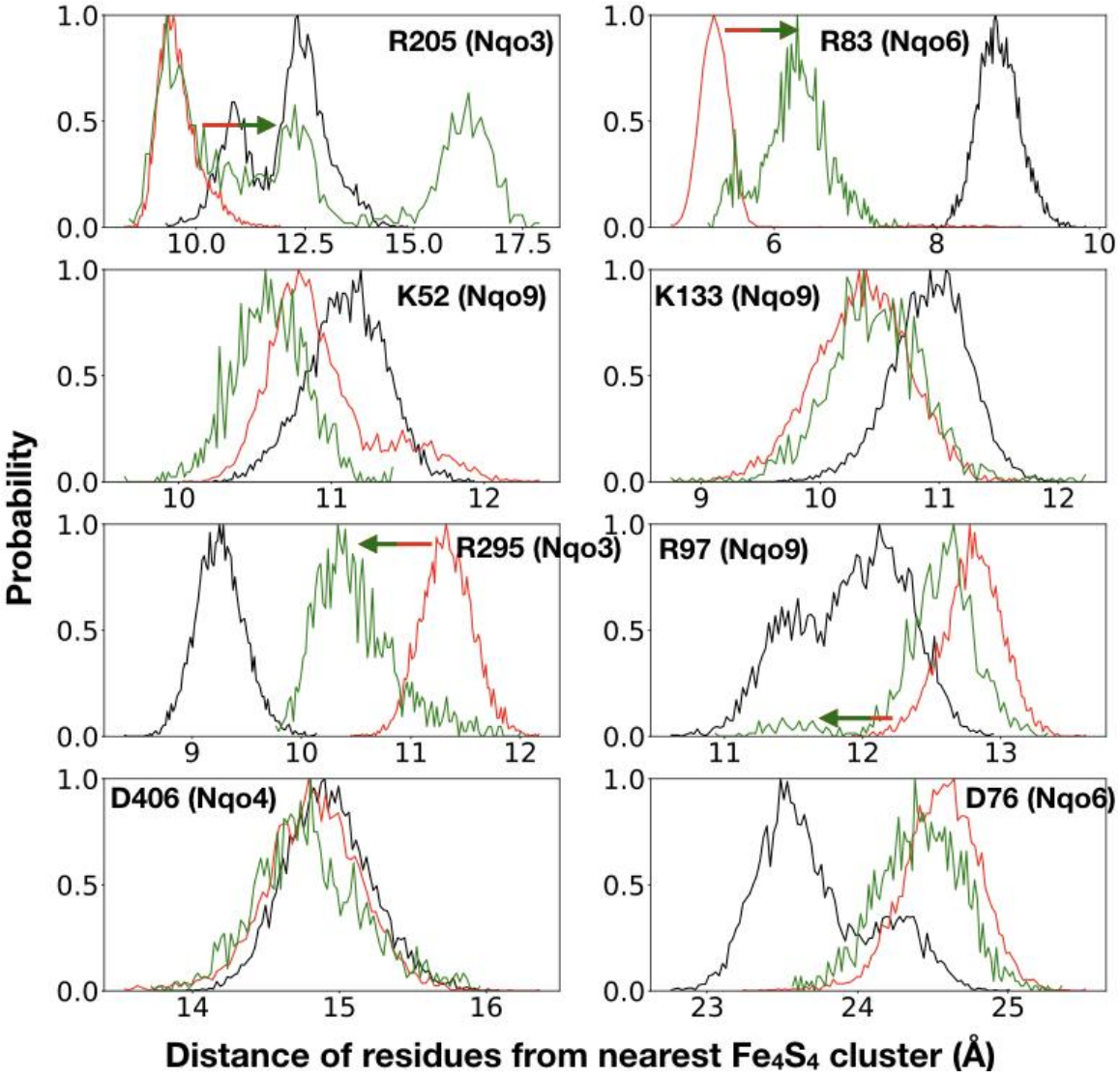

Figure S3: Distance of specific residues from its nearest iron-sulfur cluster.

Fe_4S_4 reduction causes local motion resulting in the nearby basic residues (Arg and Lys) moving closer to the closest iron-sulfur cluster (black: oxidized complex I, red: reduced complex I). Starting with the final conformation of the reduced complex I after 500 ns MD (red), simulations were continued with all the Fe-S clusters set to oxidized (green: oxidized complex I, starting from reduced). During these 800 ns simulations, basic residues (R205, R83) moved away to the Fe_4S_4 clusters. Residues R295 and R97 showed the opposite behavior as they are placed next to the N5 cluster, which remained oxidized even in the reduced complex I. The acidic residues moved away from the reduced N2 cluster, and approached it marginally in oxidized complex I, although their effect was less pronounced due to a larger distance from the said cluster. Mean and standard deviation of these distances are shown in Figure 2E of the main text.

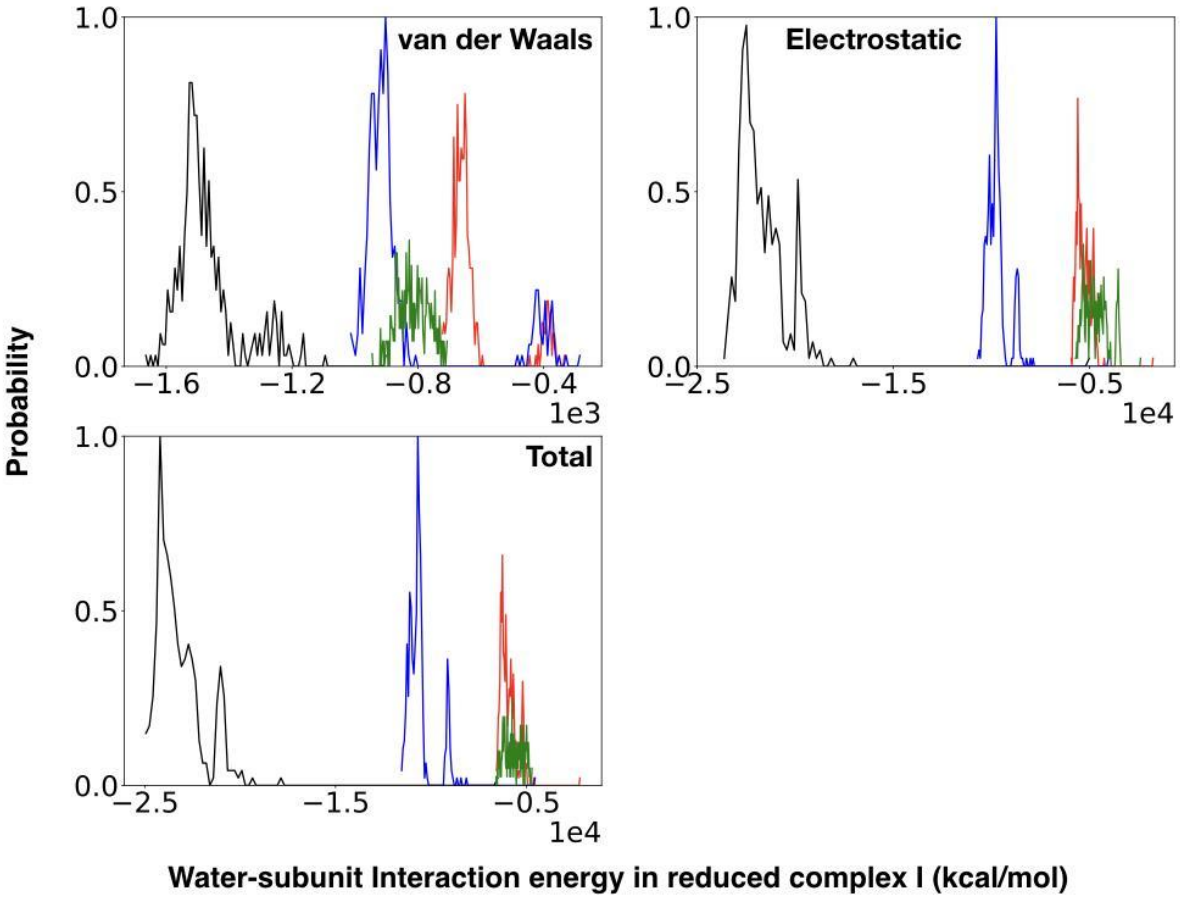

Figure S4: Water interactions of the subunits in reduced complex I.

Distribution of Interaction energies of water with subunits that undergo reorientation in reduced complex I (black: Nqo3. red: Nqo9, blue: Nqo4, green: Nqo8). Most favorable (most negative) water-interaction is experienced by subunit Nqo3, which also has the highest RMSD with respect to the initial structure (see Figure 4A). Subunit Nqo4, which houses the quinone-binding site, also experiences significant stabilization through favorable interactions with water.

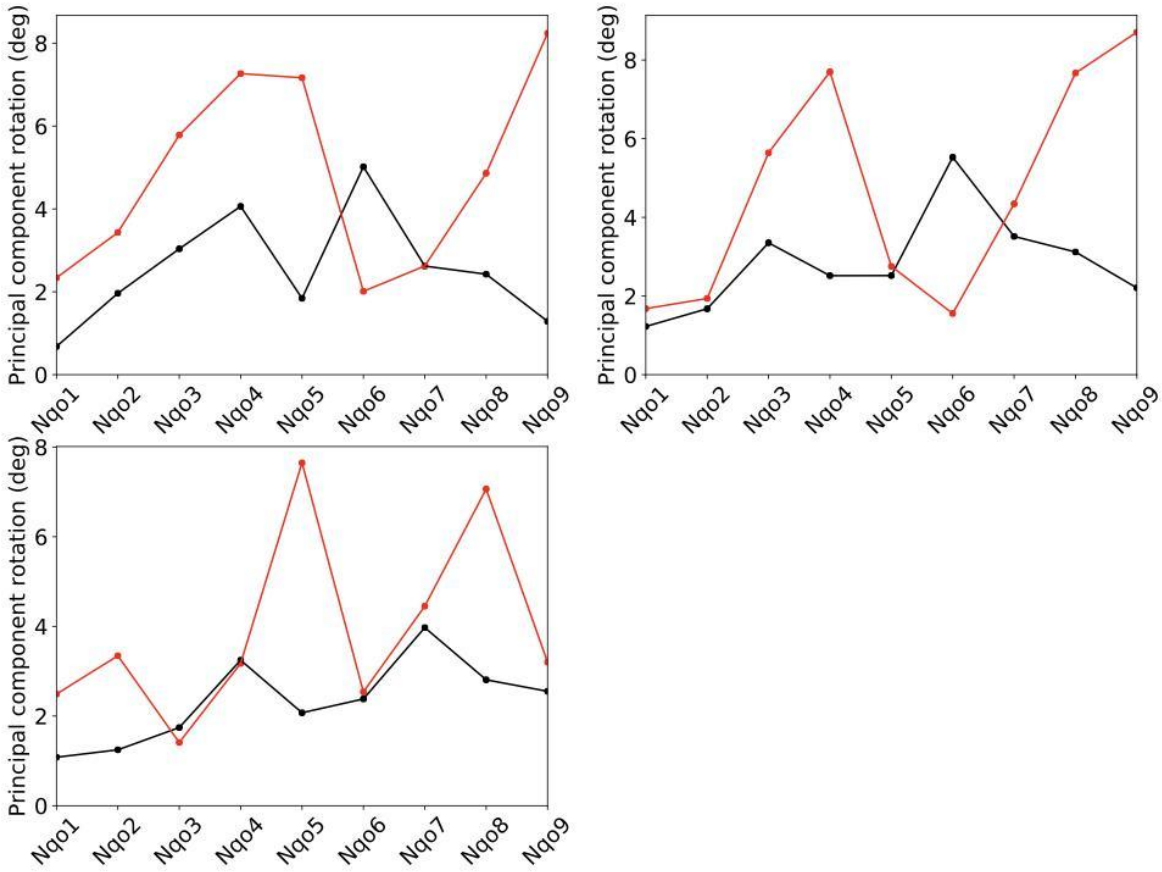

Figure S5: Change in the direction of the principal component of the subunits with respect to the initial structure.

Top left, top right and bottom left panels show, respectively, the first, second, and third principal components (black: oxidized complex I, red: reduced complex I). Reduction causes significant changes to the orientation of the domains. Most pronounced effect is seen for subunit Nqo4 along the second principal component and for subunit Nqo5 along the third principal component. The third principal component is shown in Figure 3F.

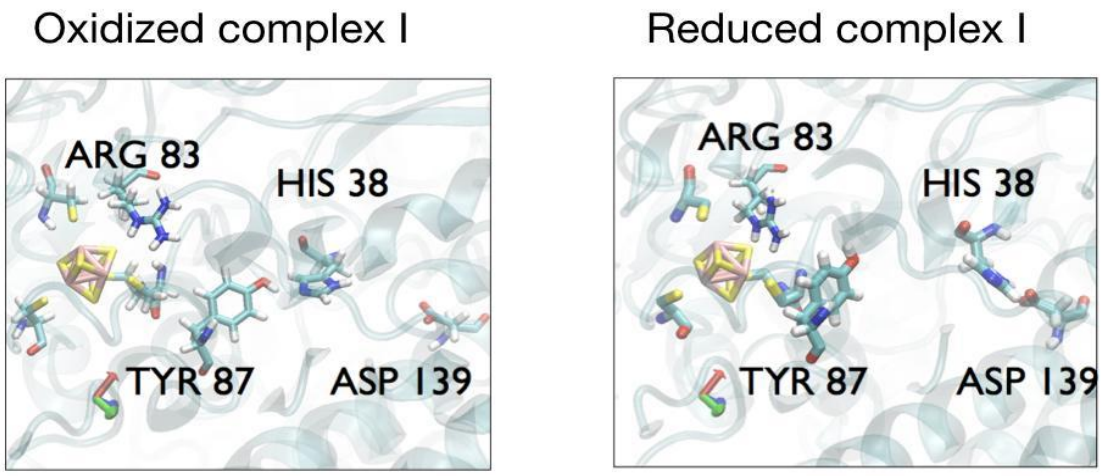

Figure S6: Arg83-mediated redox-regulation of the quinone-binding pocket of complex I.

Left: When complex I is oxidized, Arg83, identified as a switch residue in this study (see Figures 2E and S3), is away from the nearest Fe_4S_4 cluster N2. As a consequence, Tyr87 finds a hydrogen bonding partner in His38, which occludes the binding pocket. Right: When N2 is reduced, Arg83 moves closer to the latter, facilitating hydrogen bond formation with Tyr87. In this conformation, Tyr87 stays away from His38, opening the binding pocket and allowing entry of the quinone headgroup.

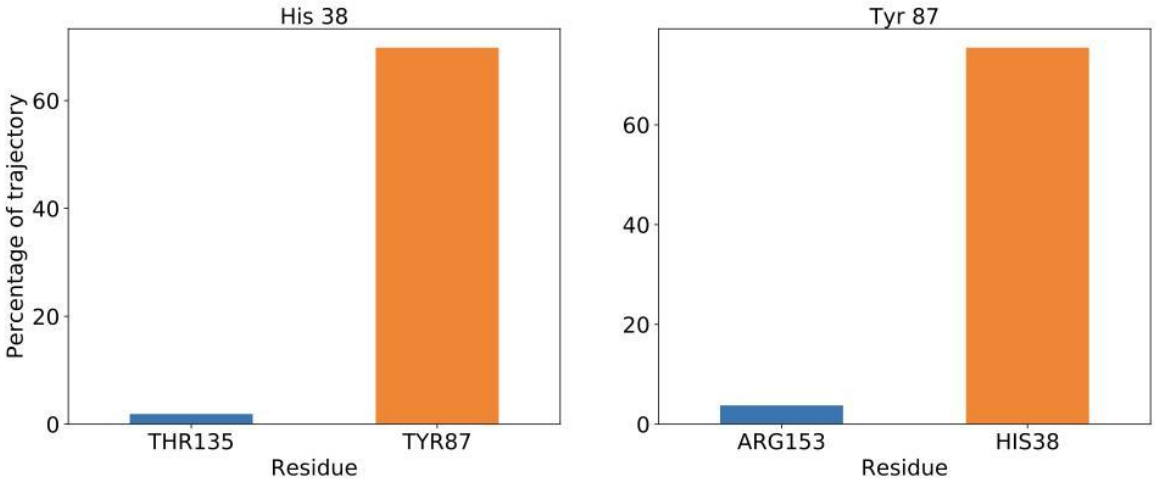

Figure S7: Hydrogen bonding between His38 and Tyr87 in oxidized complex I.

Hydrogen bonding partners of His38 (left) and Tyr87 (right) in oxidized complex I, when the binding pocket is closed. Y-axis represents the percentage of the simulation in which the said residues were hydrogen-bonded. As can be seen, His38 and Tyr87 were hydrogen bonded to each other in nearly 70% of the simulation snapshots.

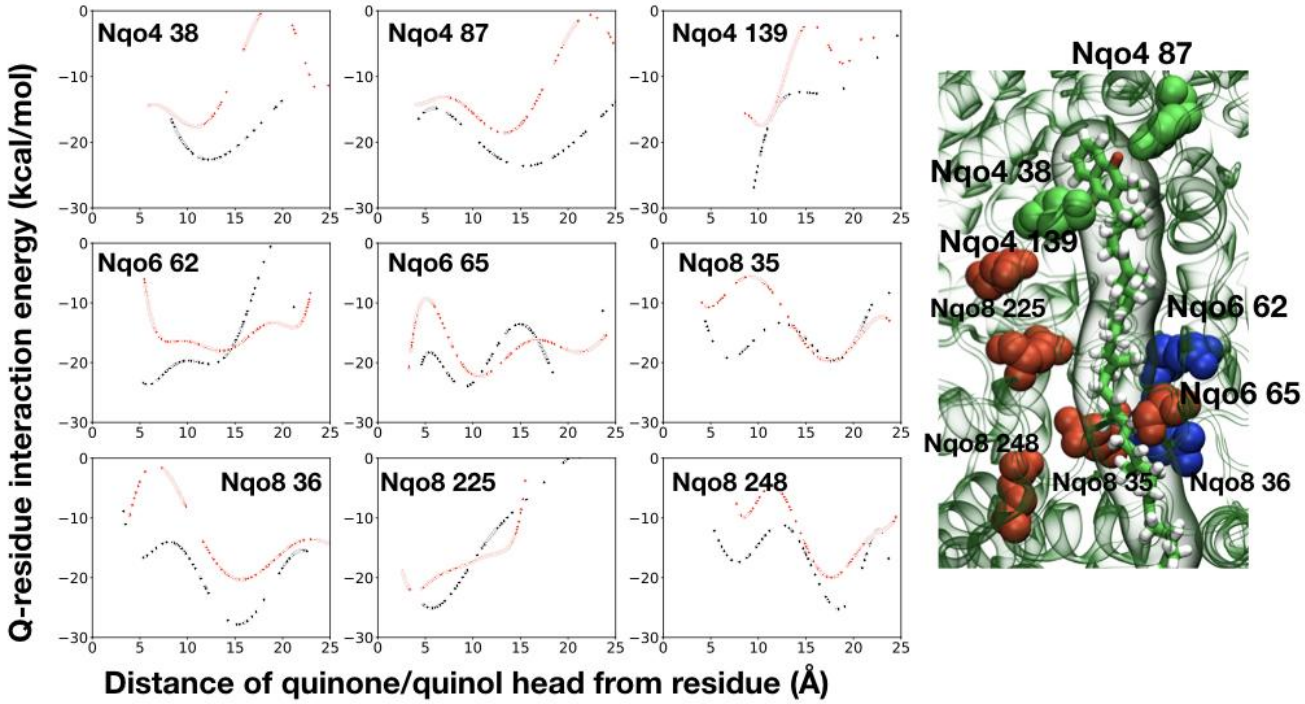

Figure S8: Quinone/Quinol-interaction with residues of the binding site and "neck" region.

Average interaction energies between the charge carrier molecule and residues comprising the quinone-binding site (top panel), and those comprising the "neck" region (middle and bottom panels) of complex I are presented as a function of the residue-head group displacement. The menaquinone interactions are presented in black and the menaquinol interactions are presented in red. The quinone-protein interactions are dominant closer to the binding pocket, while those of the quinol are more pronounced at the neck. Significant interactions remain even at higher separation distances.

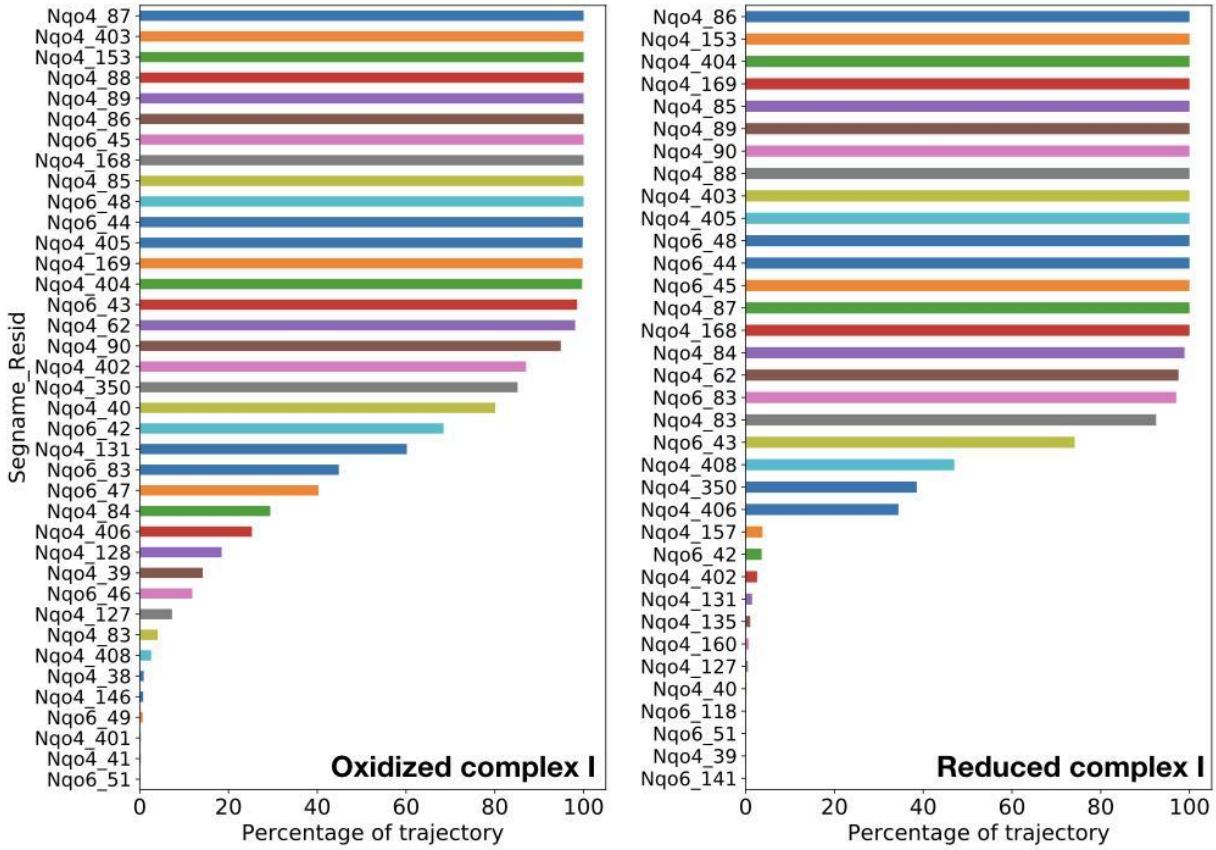

Figure S9: List of neighbors of Tyr87.

Neighbor is defined as a residue within 5Å of Tyr87, in oxidized complex I (left) and reduced complex I (right). Neighbor residues, shown along the Y-axis, are referred to as "Segname_Resid" ('Nqo4_87' refers to residue 87 of subunit Nqo4). X-axis shows the percentage of simulation snapshots where they were within 5Å of Tyr87.

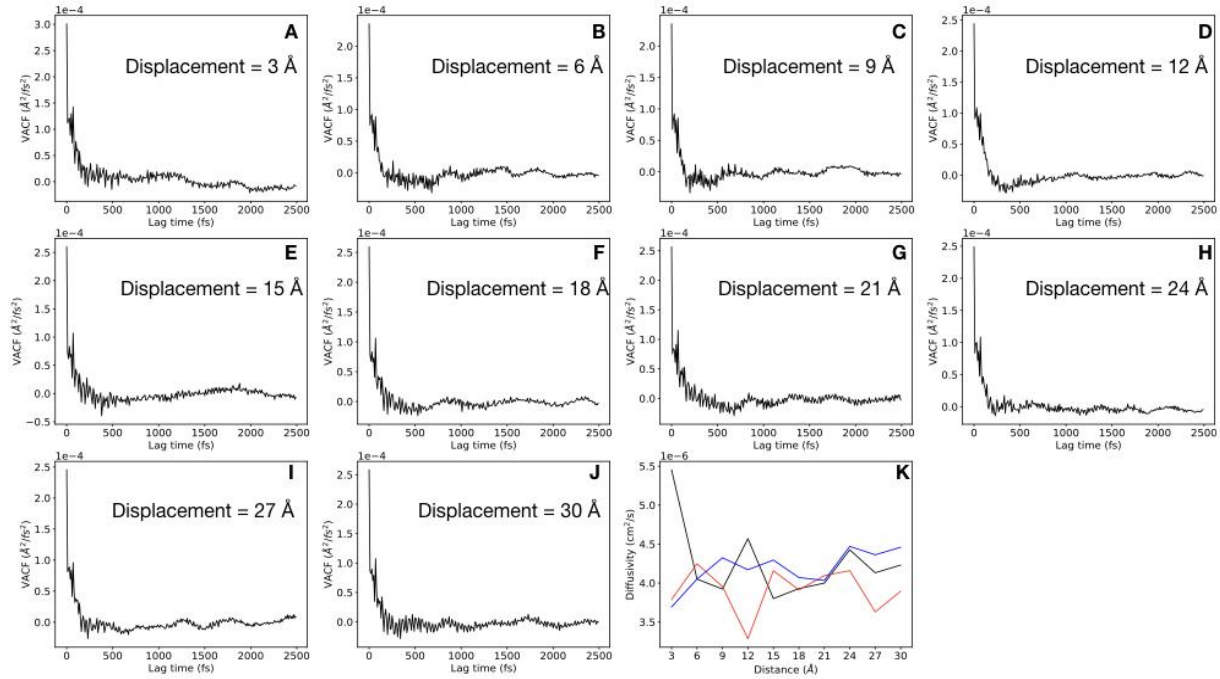

Figure S10: Position-dependent diffusion coefficient of menaquinone and menaquinol. Velocity autocorrelation function (VACF) at different quinone positions with respect to oxidized complex I are shown in panels A-J (displacement of the headgroup from the binding pocket is labeled in the inset). The VACFs were calculated from swarms of unbiased MD trajectories starting from 10 evenly spaced windows from the 30 windows used in umbrella sampling simulations. Area under the curve of the VACF was used to compute diffusivity using Green-Kubo relationship. Variations in diffusivity of menaquinone at different positions of the quinone head-group is presented in the panel K (black: oxidized complex I, red: reduced complex I). The position-dependent diffusivity profile for menaquinol within oxidized complex I is presented in blue.

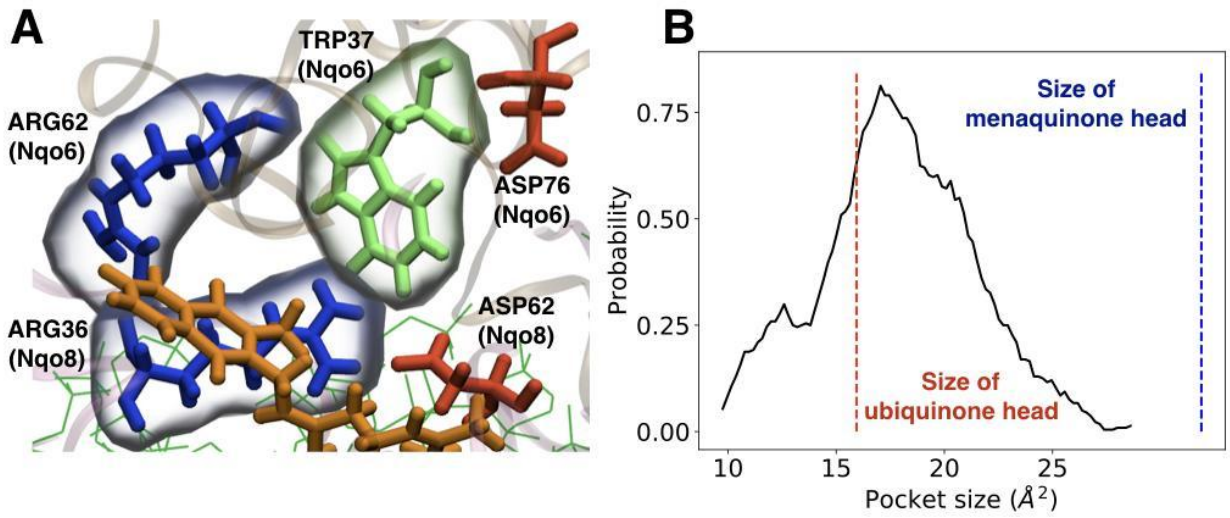

Figure S11: Comparison between ubiquinone and menaquinone.

(A) The secondary binding pocket, comprising residues Trp37 and Arg62 of subunit Nqo6 (green and blue respectively), Arg36 of subunit Nqo8 (blue). Menauinone (orange) does not interact with the said binding pocket in our simulation, and also does not interact with Asp76 (Nqo6) and Asp62 (Nqo8) unlike ubiquinone in Warnau et. al.[1] (B) Distribution of the area of the pocket described in (A) in our simulation (solid black line). Area of ubiquinone headgroup, estimated from a hexagon of 2.48 Å (this length is obtained by including the hydrogens in the ubiquinone headgroup), is 15.94 $Å^2$ (broken red line). Thus, it fits perfectly into this pocket explaining why ubiquinone interacts with the acidic residues mentioned in (A). Menaquinone headgroup, on the other hand, has an area of 31.88 $Å^2$ (broken blue line), making it too big for this pocket. Our results are also in line with those from complex II, where ubiquinone and menaquinone have distinct binding pathways, to accommodate the additional phenyl ring in the latter.[2]

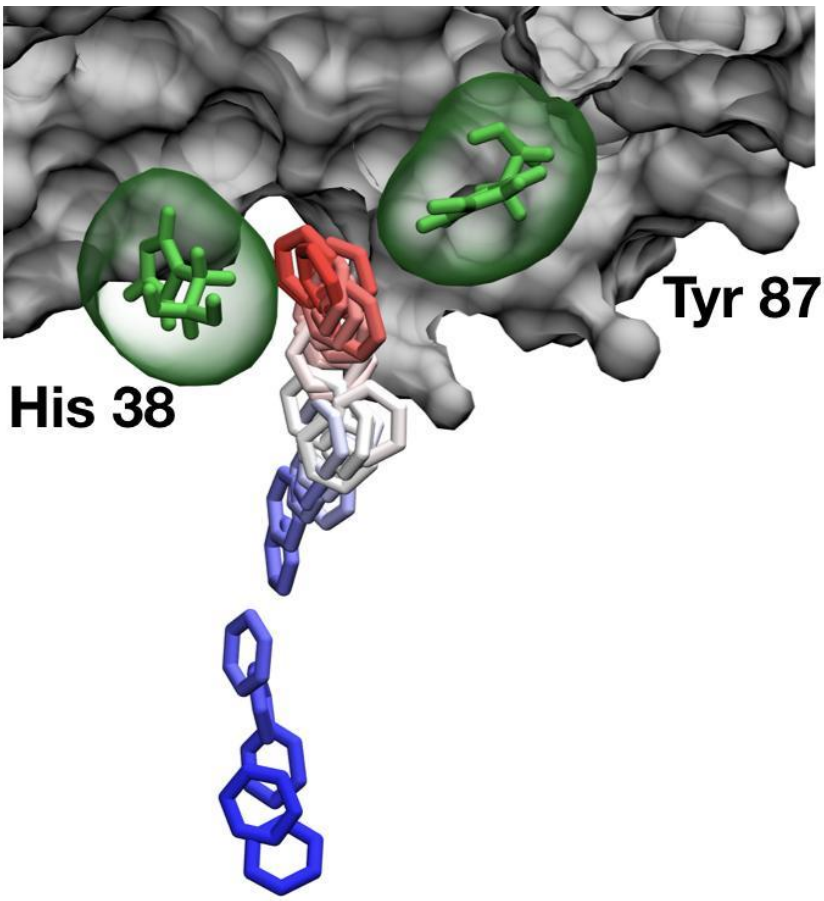

Figure S12: Sampling of the quinone-access channel.

After being docked to the binding site, quinone was pulled as described in supporting methods. Shown here are different snapshots along the quinone-access channel (quinone tail not shown for clarity). Color of the quinone head represents the time point of the pulling simulation (red: initial, close to docked structure, blue: final, far from the docked structure). His38 and Tyr87 of subunit Nquo4 that form the binding pocket are highlighted.

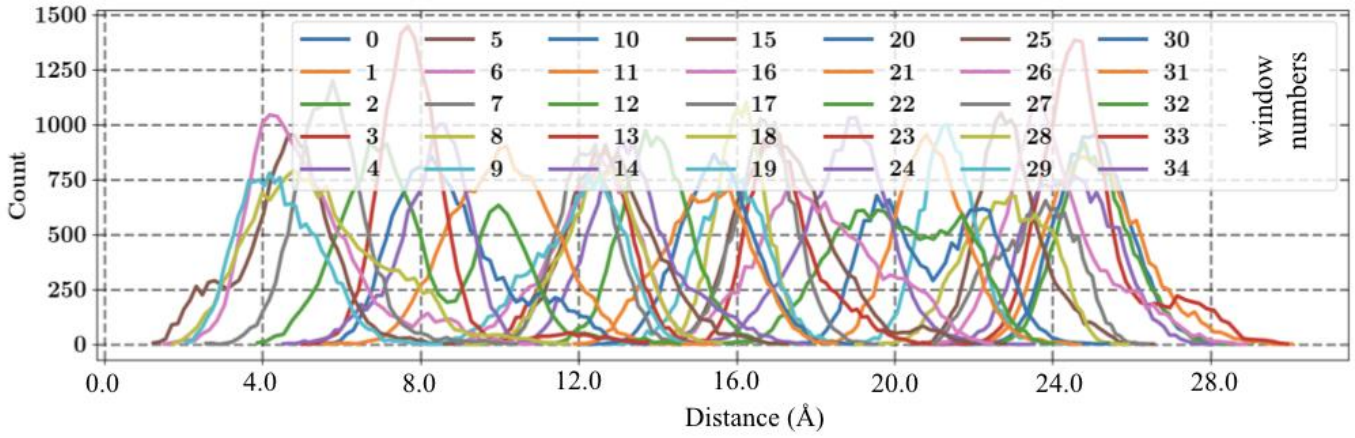

Figure S13: Histogram of reaction coordinate.

34 windows were used to sample a distance range of ~30 Å. Distribution of the distance (reaction coordinate) is shown. Overlap between neighboring windows ranged from 22% to 30%.

Segname	Resname	Resid	Charge
Nqo12	LYS	385	+1.0
Nqo12	HSE	241	0.0
Nqo12	HSE	321	0.0
Nqo12	HSE	325	0.0
Nqo12	LYS	329	+1.0
Nqo12	LYS	216	+1.0
Nqo12	ASP	166	-1.0
Nqo13	GLU	377	-1.0
Nqo13	HSE	292	0.0
Nqo13	LYS	235	+1.0
Nqo13	LYS	204	+1.0
Nqo13	GLU	123	-1.0
Nqo13	HSE	211	0.0
Nqo14	LYS	345	+1.0
Nqo14	HSE	265	0.0
Nqo14	LYS	216	+1.0
Nqo14	LYS	186	+1.0
Nqo14	GLU	112	-1.0
Nqo11	GLU	67	-1.0
Nqo11	GLU	32	-1.0
Nqo7	ASP	72	-1.0
Nqo7	GLU	74	-1.0
Nqo8	GLU	130	-1.0
Nqo8	GLU	163	-1.0
Nqo8	GLU	213	-1.0
Nqo8	GLU	248	-1.0
Nqo8	GLU	223	-1.0
Nqo8	GLU	225	-1.0
Nqo8	GLU	227	-1.0

Table S1: Protonation states of the titratable residues.

Protonation states of titratable conserved residues of subunits Nqo7, Nqo8, Nqo11, Nqo12, Nqo13 and Nqo14 in our simulations (HSE represents ε-protonated histidine).

System	System size (atoms)	Box size (Å X Å X Å)	Simulation length (μs)	Number of repetitions
Apo, all Fe-S oxidized	974512	290 X 156 X 218	0.5	3
Apo, four Fe_4S_4 reduced [N3, N4, N6a, $N2^5$]	974512	290 X 156 X 218	0.5	3
Apo, one Fe_4S_4 reduced [N2]	974512	290 X 156 X 220	0.5	1
Quinone-bound, all Fe-S oxidized	974637	276 X 145 X 239	0.5	2
Quinone-bound, four Fe_4S_4 reduced	974637	287 X 137 X 243	0.5	2
Quinol-bound, all Fe-S oxidized	974639	280 X 143 X 222	0.5	2
Quinol-bound, four Fe_4S_4 reduced	974639	286 X 146 X 229	0.5	2
Apo, all Fe-S oxidized, starting from four Fe_4S_4 reduced	974512	290 X 156 X 218	0.8	3

Table S2: List of simulation systems in this work.

Residue	ΔΔG (kcal/mol)
ARG 46 (NQ3)	1.91
ASP 132 (NQ3)	0.78
ARG 162 (NQ3)	1.59
ARG 205 (NQ3)	1.31
ARG 205 (NQ3)	0.68
ASP 215 (NQ3)	0.94
ARG 241 (NQ3)	1.27
ARG 245 (NQ3)	1.16
GLU 248 (NQ3)	1.51
GLU 439 (NQ3)	1.3
GLU 67 (NQ4)	0.7
LYS 68 (NQ4)	1.64
ARG 73 (NQ4)	1.74
ARG 84 (NQ4)	0.62
GLU 161 (NQ4)	0.87
ARG 167 (NQ4)	2.46
ARG 174 (NQ4)	1.12
GLU 185 (NQ4)	0.86
ARG 314 (NQ4)	2.42
LYS 329 (NQ4)	1.7
GLU 333 (NQ4)	2.12
GLU 352 (NQ4)	2.72
ASP 360 (NQ4)	2.16
ARG 367 (NQ4)	1.38
LYS 369 (NQ4)	1.46
ARG 371 (NQ4)	0.89
ARG 409 (NQ4)	-5.86
ARG 409 (NQ4)	-3.96
ARG 87 (NQ5)	1.87
GLU 117 (NQ5)	1.22
ARG 189 (NQ5)	2.16
ARG 193 (NQ5)	1.09
ARG 32 (NQ6)	1.38
GLU 49 (NQ6)	2.31
ASP 55 (NQ6)	-0.75
GLU 65 (NQ6)	-0.79
ARG 68 (NQ6)	-4.61
ASP 76 (NQ6)	-0.75
ARG 83 (NQ6)	2.6
LYS 87 (NQ6)	0.9
ARG 143 (NQ6)	0.82

LYS 34 (NQ9)	0.9
ARG 36 (NQ9)	3.52
GLU 74 (NQ9)	0.83
ARG 86 (NQ9)	1.84
GLU 106 (NQ9)	1.35
LYS 181 (NQ9)	-5.64

Table S3: Alanine scanning of interfacial residues of the soluble subunits of complex I.

NAMD	Phillips et al., 2005	http://www.ks.uiuc.edu/Research/namd/
VMD	Humphrey et al., 1996	http://www.ks.uiuc.edu/Research/vmd/
Gridforces/grid-steered molecular dynamics	Wells et al., 2007	http://bionano.physics.illinois.edu/node/109
APBS	Baker et al., 2001	http://www.poissonboltzmann.org
BEUS	Singharoy et al., 2016	https://doi.org/10.1021/jacs.6b01193
Generalized weighted histogram methodology	Singharoy et al., 2017	https://doi.org/10.1021/jacs.6b10744
Charmm-GUI	Jo et. al., 2008	charmm-gui.org
ProPka	Olsson et. al., 2011	https://github.com/jensengroup/propka-3.1
ROSETTA	Kortemme et. al., 2004	http://robetta.bakerlab.org/

Table S4: List of software and algorithms used in this work.

Supporting Movies

All movies are made available here:
https://drive.google.com/drive/folders/1whVOTk324M9QQ4vm1idvMaYY-nZfDo9w

3DStructureOfComplexI:

3D structure of Complex I.[3] Subunits represented by color (Nqo1: dark blue, Nqo2: dark grey, Nqo3: yellow, Nqo5: red, Nqo6: dark orange, Nqo8: green, Nqo9: pink, Nqo15: dark green, Nqo16: light blue. Nqo7, Nqo10, Nqo11, Nqo12, Nqo13, and Nqo14 shown in gray. Nqo4 not shown for clarity). Iron-sulfur clusters are shown in orange and light blue.

RedoxControlledLocalMotion:

Local effect of Fe_4S_4 reduction is demonstrated on residue Arg 189 of subunit Nqo3. Nearest Fe_4S_4 cluster (N4) is shown in orange. Simulation trajectory from oxidized and reduced complex I is overlayed. Arg 189 of oxidized complex I is shown in dark blue and that of reduced complex I is shown in light blue. As the simulation proceeds, side chain of Arg 189 moves away from oxidized Fe_4S_4 cluster, while that of reduced complex I shows no significant movement.

PocketClosesInOxidized:

Quinone-binding pocket, defined by residues His 38 and Tyr 87 of subunit Nqo4 (green), is open at the beginning of the simulation (crystal structure). Nearest Fe_4S_4 cluster (N2) is shown in blue, implying it is oxidized. As the simulation proceeds, His 38 moves away from Asp 139 (red) and interacts with Tyr 87, thus closing the pocket.

PocketOpenInReduced:

In reduced complex I (Fe_4S_4 N2 cluster shown in orange), His 38 has stable interactions with Asp 139 (red), thereby keeping the quinone-binding pocket, defined by the residues His 38 and Tyr 87 of subunit Nqo4, open throughout the duration of the simulation.

QuinoneHeadBinding:

Quinone head region binds to the pocket comprising of His 38 and Tyr 87 of subunit Nqo4 (green). Residues of the “neck” region are shown in red (acidic) and blue (basic).

QuinolNeckBinding:

Quinol interacts more favorably with the residues of the neck region, shown in red (acidic) and blue (basic). Binding pocket is shown in green.

QuinonePulling:

SMD simulation was used to pull the quinone (orange) away from the binding pocket. Subunit Nqo4, which houses the binding pocket, is shown in surface representation (blue). Transmembrane domains are shown in grey except subunit Nqo8 (green).

References

(1) Warnau, J.; Sharma, V.; Gamiz-Hernandez, A. P.; Luca, A. D.; Haapanen, O.; Vattulainen, I.; Wikström, M.; Hummer, G.; Kaila, V. R. I. Redox-Coupled Quinone Dynamics in the Respiratory Complex I. *Proc. Natl. Acad. Sci.* **2018**, *115* (36), E8413–E8420. https://doi.org/10.1073/pnas.1805468115.

(2) Maklashina, E.; Cecchini, G. The Quinone-Binding and Catalytic Site of Complex II. *Biochim. Biophys. Acta BBA - Bioenerg.* **2010**, *1797* (12), 1877–1882. https://doi.org/10.1016/j.bbabio.2010.02.015.

(3) Baradaran, R.; Berrisford, J. M.; Minhas, G. S.; Sazanov, L. A. Crystal Structure of the Entire Respiratory Complex I. *Nature* **2013**, *494* (7438), 443–448. https://doi.org/10.1038/nature11871.